

Virus Matryoshka: A Bacteriophage Particle—Guided Molecular Assembly Approach to a Monodisperse Model of the Immature Human Immunodeficiency Virus

Pooja Saxena, Li He, Andrey Malyutin, Siddhartha A. K. Datta, Alan Rein, Kevin M. Bond, Martin F. Jarrold, Alessandro Spilotros, Dmitri Svergun, Trevor Douglas, and Bogdan Dragnea*

Immature human immunodeficiency virus type 1 (HIV-1) is approximately spherical, but is constructed from a hexagonal lattice of the Gag protein. As a hexagonal lattice is necessarily flat, the local symmetry cannot be maintained throughout the structure. This geometrical frustration presumably results in bending stress. In natural particles, the stress is relieved by incorporation of packing defects, but the magnitude of this stress and its significance for the particles is not known. In order to control this stress, we have now assembled the Gag protein on a quasi-spherical template derived from bacteriophage P22. This template is monodisperse in size and electron-transparent, enabling the use of cryo-electron microscopy in structural studies. These templated assemblies are far less polydisperse than any previously described virus-like particles (and, while constructed according to the same lattice as natural particles, contain almost no packing defects). This system gives us the ability to study the relationship between packing defects, curvature and elastic energy, and thermodynamic stability. As Gag is bound to the P22 template by single-stranded DNA, treatment of the particles with DNase enabled us to determine the intrinsic radius of curvature of a Gag lattice, unconstrained by DNA or a template. We found that this intrinsic radius is far larger than that of a virion or P22-templated particle. We conclude that Gag is under elastic strain in a particle; this has important implications for the kinetics of shell growth, the stability of the shell, and the type of defects it will assume as it grows.

Dr. P. Saxena, Dr. A. Malyutin, K. M. Bond, Prof. M. F. Jarrold,
Prof. T. Douglas, Prof. B. Dragnea
Department of Chemistry
Indiana University
800 E. Kirkwood Avenue, Bloomington, IN 47405, USA
E-mail: dragnea@indiana.edu

Dr. L. He
Department of Molecular and Cellular Biochemistry
Indiana University
Bloomington, IN 47405, USA

DOI: 10.1002/sml.201601712

Dr. S. A. K. Datta, Prof. A. Rein
National Cancer Institute
P.O. Box B, Building 535
Frederick, MD 21702-1201, USA
Dr. A. Spilotros, Prof. D. Svergun
European Molecular Biology Laboratory-DESY
Notkestrasse 85, Geb. 25a, 22603 Hamburg, Germany



1. Introduction

Self-assembly of viruses, a process that brings together many copies of the viral coat protein(s) to spontaneously generate a viral shell via ordered interactions between protein subunits, has intrigued biologists and physicists alike because of its central role in the virus lifecycle and its importance in the development of viruses for applications in medicine and technology and for various antiviral therapies.^[1–5] Physical processes akin to those encountered in virus assembly are also found in many examples of supraparticles formed from inorganic nanoparticles organized through biomolecular interactions.^[6–9] While the general geometric, thermodynamic, kinetic, and mechanical rules that govern assembly and stability of symmetric, and in particular of icosahedral viruses, have received much attention,^[3,10–15] the same fundamental questions have not yet been addressed for partially ordered viruses. One such system is the immature shell of HIV-1.

In HIV-1, viral assembly occurs at the plasma membrane of the infected host cell by oligomerization of the HIV-1 structural protein, Gag, leading to budding of a non-infectious immature particle enclosed within a lipid envelope. Subsequently, Gag is cleaved by a virus-encoded protease leading to a complete rearrangement of cleaved proteins within the bud and generation of the infectious mature particle.^[16] Thus, assembly of multiple Gag proteins into immature HIV-1 primes the virus for infectivity. Understanding its underlying mechanisms is critical for exploring novel avenues for anti-HIV-1 therapy.^[17]

Early cryo-electron microscopy (cryo-EM) of immature HIV-1 purified from infected cells showed that the particles are roughly spherical and are generated in a variety of sizes ranging from 120 to 250 nm in diameter, with some regions of local order.^[18,19] A closer inspection of micrographs from individual particles revealed that native immature HIV-1 particles differ from each other with respect to their local curvature, average radius, and protein coverage at budding,^[18] suggesting that each particle really possessed its own unique topology. From theoretical studies of icosahedral virus models and spherical packings of interacting isotropic subunits, it is clear that curvature plays a major role in thermodynamic stability and the geometry of the ground state.^[20–22] However, the relationship between the geometry of immature HIV-1 and its stability and, subsequently, virus infectivity is unknown.

The Gag protein contains several flexible regions; while there are atomic structures for some domains in Gag,^[23] there is no detailed structural information on Gag itself. Gag is a 55 kDa polypeptide with three major domains: the matrix domain (MA), which is essential for Gag recruitment to the plasma membrane; the capsid domain (CA), which upon maturation forms the conical core encapsulating the viral genome; and the nucleocapsid domain (NC), which binds to the viral RNA during particle assembly.^[24,25] Gag also contains two 'linker' peptides, namely SP1 and SP2, and a small C-terminal domain, p6, all with little or no structure. While atomic structures of cleaved MA, CA, and NC domains indicate that they are largely globular, the full-length Gag protein appears to

have an unusually high aspect ratio,^[26,27] when compared with the coat proteins of other spherical viruses, and is an extended rod in immature particles.^[19] Assembly of the rod-shaped Gag protein into a roughly spherical shell presents an interesting problem since the thermodynamic ground state of a system of laterally interacting rod-shaped particles attached via their ends to a spherical surface is unknown.^[28]

The pleomorphism of immature HIV-1 particles has hampered their high-resolution structural studies since traditional structural methods all involve averaging. Pleomorphism also precluded exploration of the relationship between global structure and stability. Nevertheless, cryo-electron tomography (cryo-ET) of single particles showed that the immature lattice in all retroviruses studied to date^[29] is composed of hexamers of Gag arranged in an array with local hexagonal symmetry but whose long-range order is fraught with irregular defects in the form of large gaps and grain boundaries.^[23] Defects are required because a hexagonal lattice cannot be mapped on a spherical surface without distortion. In HIV-1, the patterns of defects varied between particles, but consistently, particles were found to contain a continuous Gag lattice with one large gap estimated to cover approximately a third of the surface area of the viral envelope.^[26] Based on this observation, a virion with a Gag shell of 130 nm in diameter is estimated to contain ≈ 2500 Gag molecules.^[30] The rim of the large gap within the hexagonal lattice is thought to be the position where the membrane of the budding, immature virus was cleaved from the plasma membrane of the host cell by the endosomal sorting complexes required for transport machinery.^[30] However, why gaps are adopted, instead of dislocations or pentameric disclinations as in the case of icosahedral viruses, and moreover, what biological role these gaps may have, is not clear.

Based on arguments borrowed from colloidal spherical packings,^[21,31] a reasonable hypothesis for the presence of gaps could be constructed on the idea of frustrated growth and consequent elastic strain leading to instability of the growing Gag shell. To test this hypothesis, an approach is needed that would alleviate the challenge for structural studies imposed by the heterogeneity of size and stoichiometry.

Advances in sub-tomogram averaging techniques have determined the structure of immature HIV-1 particles at sub-nanometer resolution, revealing tertiary and quaternary interactions that mediate assembly in HIV-1.^[32] However, translating local interactions into global packing properties is challenging. For instance, the intrinsic curvature of the hexameric Gag subunit presumably plays a role in the magnitude of bending strain and overall stability of the growing hexagonal lattice,^[33] however, the intrinsic radius of curvature of Gag hexamers in absence of nucleic acid is not known (although well-defined potential ranges for this value may be indicated by previous studies).

Recently, hybrid cryo-EM and cryo-ET of tubular assemblies of Gag, assembled *in vitro* from recombinant Gag proteins, were successfully employed to determine the assembly state structure of Gag with 8 Å resolution.^[34,35] To reduce size heterogeneity, only tubes with similar diameters and helical symmetry were selected for processing.^[34] However, because the side of a cylinder is a surface of zero Gaussian curvature,

tube assemblies were solely formed from hexamers of Gag. Geometric frustration is absent; gaps were not observed. To include effects of elastic strain on particle structure, and to study the origin and potential functional properties of gaps in immature HIV-1, a different approach is required.

The task at hand was facilitated by a previously described templated assembly approach in which recombinant HIV-1 Gag protein was assembled around ssDNA-derivatized gold nanoparticles to generate virus-like particles (VLPs).^[36] The use of a template significantly reduced the size polydispersity of the assembled VLPs. Specifically, 60 nm gold nanoparticles were found to be the most efficient for generating homogeneous Gag VLPs. However, while broad morphological features of the Gag shell assembled on gold nanoparticles appeared to mimic those of authentic immature HIV-1, these VLPs were not amenable to detailed structural analysis using cryo-EM since the electron-dense gold core strongly absorbed and scattered electrons, obscuring any signal from the Gag lattice.^[37] Moreover, colloidal metal nanoparticles are not strictly monodisperse, exhibiting, on average, a 10% variation in size.

In this study, we present a novel approach to these problems (**Figure 1a**) in which Gag was assembled on a monodisperse, electron-transparent template derived from the Enterobacteria phage P22. Genetic manipulation, recombinant expression, self-assembly, and surface morphology of P22 are well-established,^[38] making it an excellent candidate for use in nanotechnology. When expressed in *E. coli*, in the presence of scaffolding proteins of P22, the P22 coat proteins assemble into an icosahedral $T = 7$ procapsid structure comprising 420 identical subunits.^[39] As far as we know, these procapsids are identical to each other at the atomic level. P22 procapsids have an outer radius of ≈ 30 nm, which is slightly smaller than the average inner radius of wt immature HIV-1

Gag shells (35 nm), but close to the lower limit of the distribution of inner radii observed in wt immature HIV-1.^[40] Through the use of P22 procapsid VLPs as a template, tight control is imposed on the size and shape of Gag assemblies, thereby generating reproducible uniform curvature (and hence packing defects) in VLPs of immature HIV-1.

A Gag-derived protein, Δ MA-CA-NC-SP2 (or Δ 16-99Gag,^[41]) has been previously shown to assemble in vitro into spherical VLPs that are virtually indistinguishable, in terms of structural organization, from native immature HIV-1 particles.^[42] The primary sequence of Δ MA-CA-NC-SP2 is identical to wt Gag apart from two deletions: one in the globular part of the MA domain (residues 16–99) and the other consisting of the entire p6 domain (52 residues). The deletion within the MA domain facilitates the assembly of Gag in solution.^[43] The second mutation, i.e., deletion of the p6 domain at the C-terminal of Gag, has been incorporated to prevent degradation of the protein in bacterial hosts during recombinant protein production^[43] and does not affect Gag assembly.^[42,44] Since Δ MA-CA-NC-SP2 offers improved yields of recombinant protein and a higher efficiency of assembly in vitro without affecting the morphology of assembled particles, all the work described in this paper was conducted using Δ MA-CA-NC-SP2, referred to as Δ MA-Gag (**Figure 1b**).

We have now analyzed the VLPs formed by Δ MA-Gag on P22-derived templates. Our main findings are: (i) P22- Δ MA-Gag VLPs show a far narrower size distribution than any previously described Gag-derived structures. (ii) Analysis of the cryo-EM density distribution from VLPs reveals radial domain structure and ordered lateral packing consistent with structural data obtained from wt HIV-1 particles by cryo-ET. (iii) Unlike previously described HIV-1 VLPs, these VLPs do not contain observable gaps. (iv) The length and polarity of the nucleic acid linking the Δ MA-Gag lattice to the P22 core have a dramatic influence on the assembly efficiency and final coverage, respectively, of the VLPs, but do not significantly affect the outer diameters. (v) If this linker is digested with a nuclease in assembled VLPs, the VLPs expand to a different average curvature through the occurrence of gaps, remaining in a metastable state for hours; these observations demonstrate the presence of attractive forces between Gag molecules in the assembled state.

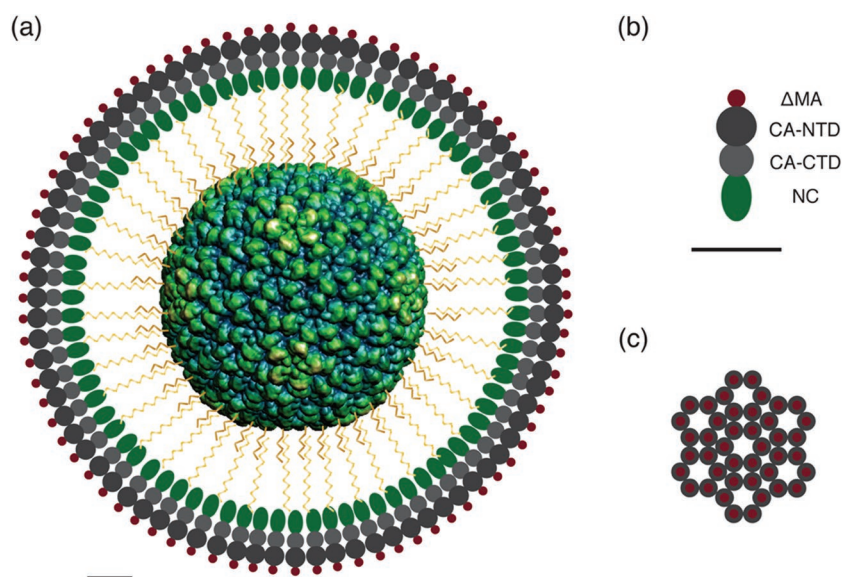


Figure 1. Schematic representation of template-directed assembly of Δ MA-Gag. a) Δ MA-Gag molecules assembled on the surface of a P22 procapsid functionalized with strands of ssDNA (shown as yellow zig-zag lines). Δ MA-Gag domains have been drawn to scale using size estimates from domain structures published from cryo-EM studies of Δ MA-Gag (flexible spacer peptides not shown). Scale bar = 10 nm. b) Schematic of Δ MA-Gag drawn to scale. Scale bar = 10 nm. c) Schematic depicting the top view of a Δ MA-Gag hexagonal lattice.

2. Results

2.1. Generation of Templates and Assembly of Δ MA-Gag

Authentic retroviral particles always contain RNA and, in vitro, the efficiency of Gag assembly into VLPs is profoundly enhanced by the presence of nucleic acids.^[44] While in infected cells, assembly of Gag occurs around the dimeric HIV-1 genomic RNA.^[44,45] Gag can assemble in

vitro on a wide variety of RNAs and short DNA oligonucleotides.^[44] This assembly is driven by non-specific electrostatic interactions between the nucleic acids and the basic residues of the NC domain.^[23] Nucleic acids are likely to act as a scaffold for Gag multimerization by recruiting subunits and promoting concentration-dependent intermolecular Gag–Gag interactions. Recently, it was suggested that the RNA content controls the size of immature HIV-1 particles.^[46]

In order to generate templates for assembly of Δ MA-Gag in vitro, P22 procapsid VLPs were functionalized with DNA. To this end, P22 procapsids were genetically engineered to express surface cysteines by incorporating a point mutation, M338C, in its coat protein (Supporting Information Figure S1). In addition, native surface lysines on P22_M338C VLPs were functionalized using chemical crosslinkers to generate several free thiol groups on the procapsid surface (see methods). Thiol groups from the genetically engineered surface cysteines and functionalized surface lysines were chemically bound to strands of ssDNA via a maleimide linkage. This ssDNA was the 12 nt long sequence: 5'-ACACACACACAC-3' or 5'-(AC)₆-3' with a modifiable amine group at the 5' end. Optimization of reaction conditions was achieved using dye-labeled (AC)₆ strands and the efficiency of labeling was quantified from relative absorbance values of the coat proteins (at 280 nm) and ssDNA-fluorescein dyes (at 495 nm). By modulating the molar ratios of P22_M338C and (AC)₆, the average labeling efficiency of procapsids achieved in separate experiments was between 70 and 290 ssDNA strands per shell. Differential single particle reconstructions from cryo-EM of labeled and unlabeled procapsids showed negligible differences in DNA coating between the hexamers and pentamers in the icosahedral P22 lattice (Supporting Information Figure S2a). While no bias in labeling was observed between different sites on the procapsid, not much can be said at the moment about the structure adopted by the ssDNA away from the procapsid surface.

Charge-detection mass spectroscopy (CDMS) of two batches of P22_M338C labeled with \approx 160 ssDNA/shell and \approx 225 ssDNA/shell showed an expected change in mass due to presence of \approx 160 and \approx 225 (AC)₆ ssDNA per shell, respectively. The full width at half-maximum (FWHM) values of each CDMS spectrum were similar to the FWHM value of the unlabeled P22_M338C spectrum, showing that the variation in labeling within a sample was no more than the inherent heterogeneity of the unlabeled P22_M338C sample (Supporting Information Figure S2b). Together, these results indicate that covalent attachment of ssDNA on P22_M338C allows for close control of ssDNA coverage.

The principal RNA in wt HIV-1 is a dimer of genomic RNA, with a total size of \approx 19 kb. To generate a template with sufficient surface charge density for Gag assembly, the (AC)₆ strands on P22_M338C-(AC)₆ were hybridized with a second, longer strand of ssDNA using base pair complementarity. The sequence of this second strand was designed to be of (GT) repeats; a portion of this ssDNA paired with the (AC)₆, while the rest remained unpaired and thus, available for binding to the NC domain of Gag. Unhybridized ssDNA was removed from the reaction by size exclusion chromatography.

Adjustments in surface charge density by varying the sequences, lengths, and coverages of both strands of DNA allowed for a systematic study and optimization of the nucleic acid content required for efficient assembly of Δ MA-Gag on P22-derived templates (Supporting Information Table S1).

Purified recombinant Δ MA-Gag was assembled on templates by adding Δ MA-Gag at concentrations above saturation to the ssDNA-labeled procapsid templates. Assembly was allowed to proceed under conditions adapted from the protocol by Datta and Rein.^[43] Assembly efficiency was assessed by examining EM images and scoring the fraction of P22 particles that appeared to be completely encased in a shell of Δ MA-Gag. A nucleic acid:Gag ratio of 3%–5% (w/w) was found to be optimal for assembly (Supporting Information Figure S3). Conditions that did not support any assembly were evident from the presence Gag aggregates and bare P22 templates in EM images (Supporting Information Figure S3 Inset).

An assembly efficiency of >80% was routinely achieved when P22_M338C was labeled with 153.8 ± 20 strands of (AC)₆ (as measured from absorbance values), and when each (AC)₆ was hybridized with a second ssDNA of 80 nucleotides of the following sequence: 5'-(GT)₁₀(GGTT)₁₅-3'. In this case, each procapsid VLP displays on an average: $153.8 \times (12 + 80) = 14150$ nucleotides, each contributing one negative charge. This is of the same order as that seen in wt HIV, where the two strands of genomic RNA (\approx 19 400 nucleotides in total) initiate Gag assembly. However, assuming a quasi-radial arrangement for the ssDNA, nucleotides closer to the procapsid may be less “exposed” to Gag binding than the nucleotides at the periphery. The distribution of accessible nucleotides in this system is presumably different from what would be expected in, e.g., a free string of viral RNA in solution. A partially extended RNA may display a lower overall charge density versus the relatively localized nature of the radially arranged ssDNA in this system.

2.2. Morphological Characterization of P22- Δ MA-Gag VLPs

Small angle X-ray scattering (SAXS) was employed to investigate the potential existence of a dominant structure of P22- Δ MA-Gag VLPs, in close-to-native aqueous environments. We envisaged that SAXS would determine a single type of mesoscopic defect, for instance, a grain boundary scar as seen in the case of a nematic liquid crystal on the surface of a sphere,^[47] or large gaps between regular bunches of subunits as seen in assemblies of anisotropic rod-shaped molecules attached at one end.^[28,48]

The scattering patterns of P22 procapsids (without Δ MA-Gag) suggested that their radius of gyration (R_g) was 26 ± 1 nm and their maximum size (D_{max}) was 60 ± 3 nm, values that agree closely with those published from the EM model of the P22 procapsid (PDB entry: 2XYY.^[49]). The scattering curve of P22 VLPs (Figure 2a) displayed a series of clear maxima confirming the isometric structure of P22 procapsids. The scattering curve computed from the EM model of the procapsid (dashed line in Figure 2a) showed a similar, yet more pronounced, sequence of maxima.

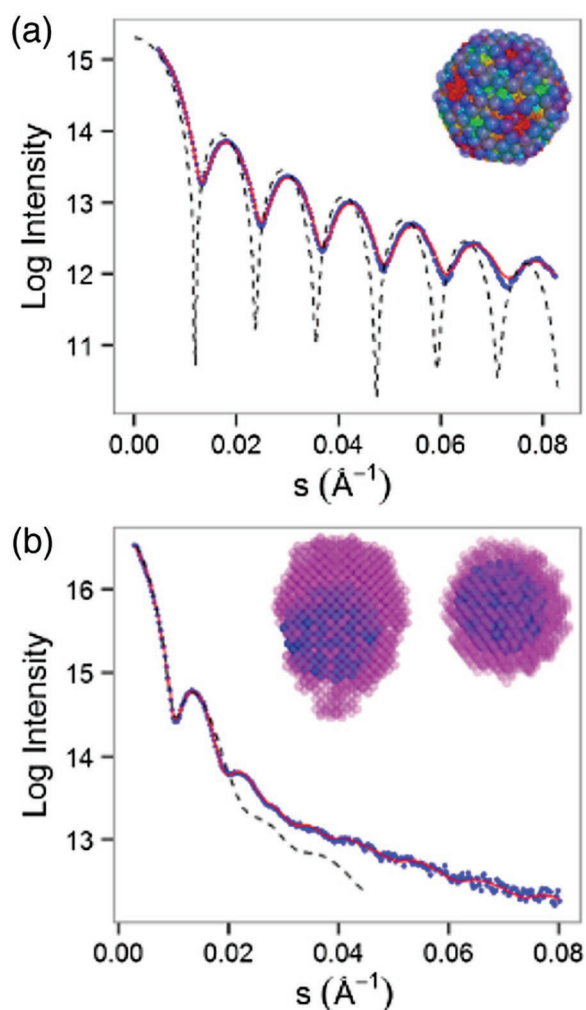


Figure 2. SAXS analysis of P22- Δ MA-Gag. a) Scattering patterns of P22 VLPs (blue dots), a fit from its ab initio model (red curve) and the intensity calculated for the published atomic model (dashed line; PDB: 2XY). The inset shows the two models superimposed: transparent beads represent the ab initio model and space-filling colors represent the atomic model. b) Scattering from P22- Δ MA-Gag VLPs (blue dots), a fit from the ab initio model (red curve) and the best-fit model for scattering computed for polydisperse hollow spheres (dashed line). The inset shows two orthogonal orientations of the ab initio model.

For P22- Δ MA-Gag VLPs, the scattering patterns (Figure 2b) gave larger overall parameters ($R_g = 35 \pm 2$ nm and $D_{max} = 95 \pm 3$ nm). Thus, the difference in sizes between the P22 templates and the P22- Δ MA-Gag VLPs is ≈ 35 nm, which corresponds well with the expected length of the two Δ MA-Gag molecules. The scattering pattern of P22- Δ MA-Gag VLPs contained fewer features compared to those of P22 procapsids, which suggests that the VLPs are either hollow spheres with limited polydispersity or are monodisperse but anisometric. We found that the scattering patterns can be reasonably fitted (at low resolution) to a simple

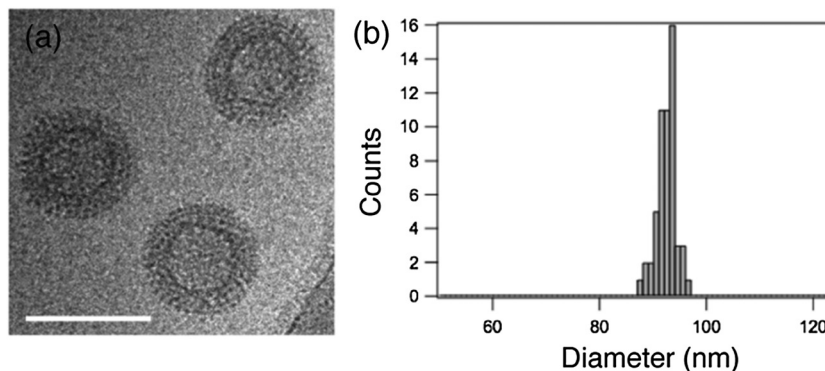


Figure 3. Cryo-EM of P22- Δ MA-Gag. a) VLPs imaged by cryo-EM at a magnification of 40 000 \times . Scale bar = 100 nm. b) A histogram of the size distribution of diameters measured from 55 P22- Δ MA-Gag particles.

model of polydisperse hollow spheres with an inner diameter of 15 nm, outer diameter of 42 nm and a Gaussian size distribution with FWHM of 6 nm (dashed line in Figure 2b).

To visualize the organization of the VLP, ab initio bead models were generated by simultaneously fitting scattering data from P22 and P22- Δ MA-Gag VLPs. The bead model (inset of Figure 2b) show P22 (blue-colored beads) encapsulated inside a Gag shell (magenta-colored beads), of a thickness we expect from molecules attached at one end and interacting laterally.^[16] However, the average Gag shell appears asymmetric. This is because the ensemble SAXS measurement averages any differences between shells of different particles and even within the shell of a single particle. Thus, incompletely coated particles or particles with the coat partially peeling off, will contribute to the anisotropy as the model was reconstructed without any assumptions.

To avoid average among dissimilar particles within the sample, and to examine the nature of defects, cryo-microscopy of P22- Δ MA-Gag VLPs was undertaken. Typical cryo-EM images showed radial layering and periodic striations along the particle circumference (Figure 3a). The average VLP diameter measured for over 50 particles by cryo-EM was 92.4 ± 1.8 nm (Figure 3b); this is a far narrower size distribution than that ever seen with wt immature HIV-1 particles (169 ± 29 nm)^[18] or Δ MA-Gag VLPs assembled in vitro on yeast tRNA molecules (140 ± 23 nm).^[18] The symmetry of the P22 procapsid was evident from cryo-EM images but its icosahedral lattice did not influence the sphericity of P22- Δ MA-Gag VLPs to any measurable extent. This is not unexpected, considering the minimal amount of faceting in P22 VLPs, and the long, flexible ssDNA linker between the P22 procapsid and Δ MA-Gag.

The morphological uniformity of P22- Δ MA-Gag VLPs enabled us to examine structural features of the Gag lattice in considerable detail. Fourier transform analysis of striations along the circumference of a circle drawn at a radius of 400 \AA from the particle center for 10 randomly selected P22- Δ MA-Gag VLPs yields a prominent peak at 0.0148 \AA^{-1} (Figure 4). This peak corresponds to a main spatial period of 67.5 \AA . The ratio between the spatial period of striations (67.5 \AA) and the radius of the circle where measurements

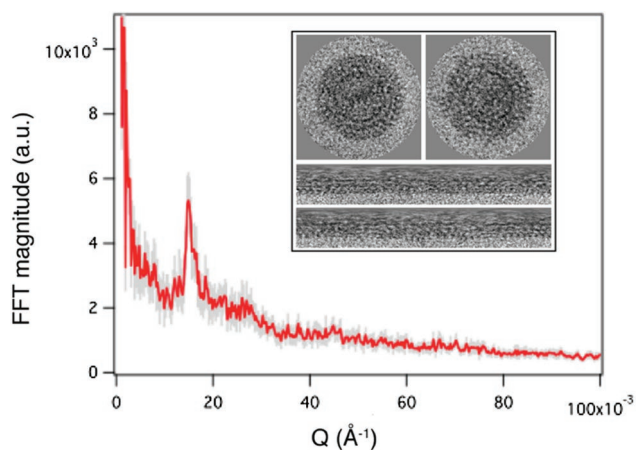


Figure 4. Fourier transform of Gag intensity in P22- Δ MA-Gag. The average FFT wave (shown in red) of the intensity profiles obtained for the 10 randomly picked P22- Δ MA-Gag particles at a radius of 405 Å from the particle center. Inset: Representative images, and rectangular strips generated for particles by converting the image into polar coordinates using Spider:PO. An inner radius of 2 pixels (6 Å) and an outer radius of 200 pixels (600 Å) from the center (0,0) were selected.

were taken (400 Å) is 0.168, which agrees closely with the corresponding ratio in wt immature HIV-1, where a lattice spacing of 80 Å is observed for an average particle radius of 500 Å (80:500 = 0.16).^[32] We compared the ratio and not the absolute value for lattice spacing since Gag is radially oriented and the circumferential spatial periods will depend on the radial location at which the measurement was taken.

A simple center alignment of the images from 260 P22- Δ MA-Gag VLPs and subsequent particle averaging directly led to a clear view of the radial organization of protein domains (**Figure 5a**). This would not be possible in any of the other available models for immature HIV-1, such as Δ MA-Gag VLPs assembled in vitro on yeast tRNA (Supporting Information Figure S4a), because variations in VLP diameters and in local radii of curvature would lead to blurring of features (Supporting Information

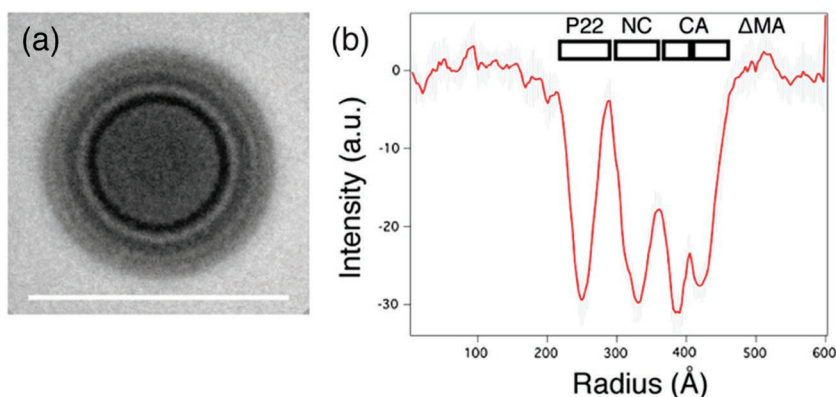


Figure 5. Radial density profile of P22- Δ MA-Gag. a) An average image obtained by superposing cryo-electron images of 260 P22- Δ MA-Gag particles using EMAN1. Scale bar = 100 nm. b) Radial profile for P22- Δ MA-Gag (red) obtained from averaging the gray intensity profiles of 10 individual P22- Δ MA-Gag particles. The horizontal axis shows distance from the particle center in Å.

Figure 4b). In previous studies with VLPs of immature HIV-1 generated in vitro, extraction of radial organization was only possible after several further processing steps and assumptions.^[19]

The P22 template plays the role of an internal spatial standard in our approach since its thickness and outer diameter are known. This facilitates interpretation of the radial density profile in terms of Gag domain organization (Figure 5b). The dark rings of Figure 5a correspond to the minima in Figure 5b. Minima locations are consistent with previously reported placement and radial extent of Gag domains in Δ MA-Gag VLPs^[18] and in the CA-NC portion of immature HIV-1 particles.^[23,40] Moreover, the radial layering and periodic striations along the circumference of P22- Δ MA-Gag VLPs are consistent with reported structural characteristics of an authentic immature HIV-1 particle. Thus, at least at a local level, Gag-Gag arrangements in P22- Δ MA-Gag VLPs appear to be indistinguishable via routine methods from those in wt particles.

2.3. Modification of Templates to Establish Factors Affecting Gag Assembly

The templated assembly approach provides a systematic framework for identification of conditions that allow efficient assembly of Δ MA-Gag. To this end, P22-derived templates were functionalized with different lengths, sequences, and coverages of ssDNA and the efficiency of assembly was scored (Supporting Information Table S1). It was found that deviations in the length and surface coverage of DNA outside an optimum window led to reduced efficiency of assembly, and ultimately to failure of assembly. Specifically, optimal efficiency for assembly was observed at a number density of $\approx 153.8 \pm 20$ ssDNA/shell and a length of 60–100 nucleotides for the second strand of DNA (Supporting Information Table S1). A two-fold reduction in the number of (AC)₆ strands attached to P22 VLPs (≈ 80 ssDNA/shell) reduced the efficiency of Δ MA-Gag assembly significantly. On the other hand, an increase in the number of (AC)₆ strands attached to P22 VLPs (≈ 225 ssDNA/shell) also led to reduced Δ MA-Gag assembly.

In the conditions of Figure 3, where major gaps could not be observed, it is reasonable to assume that Δ MA-Gag subunits completely cover the surface of the P22 template. A P22- Δ MA-Gag VLP of diameter = 92 nm (Figure 3b) is then estimated to comprise ≈ 2640 Gag molecules or 440 Gag hexamers (since the surface area of a 92 nm spherical VLP is ≈ 26580 nm² and that of a hexameric Gag subunit = ≈ 60 nm²). Therefore, P22 procapsids labeled with 153.8 ssDNA (14150 nucleotides) roughly provide ≈ 5 nucleotides/Gag molecule. This value is comparable to that calculated for an authentic retrovirus particle (≈ 4 bases/Gag molecule), which would contain ≈ 5000 Gag

molecules (if there were no gaps)^[50] and a dimeric genomic RNA of $\approx 19\,400$ nucleotides. Gag has also been shown to bind ≈ 4 bases/molecule *in vitro*, using surface plasmon resonance binding assays.^[51] However, these comparisons must be made with caution since differences are expected in the morphologies of procapsid-bound ssDNA and free genomic RNA in the cell.

Because the sequence of the synthetic ssDNA linker was specified, we could also control its orientation relative to the P22 core. Somewhat surprisingly, we found that this variable had a profound effect on the quality of VLP assembly. Thus, we compared assembly using the sequence: 5'-(GT)₁₀(GGTT)₁₅-3' and its reverse sequence: 5'-(TTGG)₁₅(TG)₁₀-3'. The 5' portion of the former sequence hybridizes to the (AC)₆ strands, while the latter sequence hybridizes to them with its 3' end. As a result, in the first case, the unpaired ssDNA points inward, toward the procapsid surface, while in the second case, the unpaired ssDNA points outward, away from the procapsid surface. Templates were generated by hybridization of P22_M338C-(AC)₆ with the inward (GT) and outward (TG) strands and used for the assembly of Δ MA-Gag.

Assuming that in both cases every (AC)₆ strand hybridized with a second strand, the two templates were expected to have the same mass and charge differing only in the orientation of the unpaired DNA. We analyzed both templates (before addition of Δ MA-Gag) by agarose gel electrophoresis, and found that the templates with “outward” ssDNA migrated slower than those with “inward” ssDNA (Supporting Information Figure 5). This suggested that the two templates, differing in the orientation of their ssDNA, had different effective outer diameters. Surprisingly, despite these differences in the chromatographic size of templates, when the VLPs formed by addition of Δ MA-Gag to these templates were analyzed, we found that the P22- Δ MA-Gag VLPs had the same average diameter (Figure 6a–c). Moreover, the Gag coverage was different in both cases: In the case of outward ssDNA, around 50% of the P22- Δ MA-Gag VLPs appeared to have partial shells of Δ MA-Gag (Figure 6b). For the inward orientation of DNA, a striking feature of P22- Δ MA-Gag VLPs, which is in sharp contrast with native immature particles, is the absence of any visible gaps within the Gag lattice. While this feature contributes to the high reproducibility of P22- Δ MA-Gag VLPs, it also gives rise to the intriguing question of how curvature is achieved in the absence of large gaps. The arrangement of individual Gag subunits by which closure of the Gag lattice was achieved at these high coverages will be addressed in detail by cryo-ET in a separate report.

Could the difference in Δ MA-Gag coverage be due to the fact that there is less DNA on the outward template due to poor efficiency of hybridization? CDMS measurements disproved this possibility: both templates were found to be similar (within 10%) in mass (Supporting Information Figure S6). Comparison of the relative lengths of protein domains in the schematic shown in Figure 1a and the experimental data shown in Figure 3 suggest another possibility. The NC domain of Gag has been shown to have non-specific nucleic acid chaperone activity^[52] and it is evident from cryo-EM of

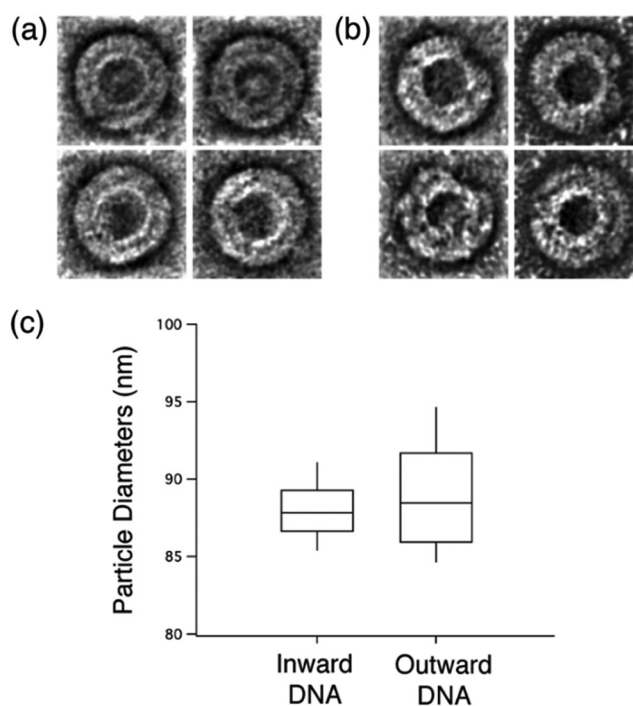


Figure 6. Effect of ssDNA polarity on assembly of P22- Δ MA-Gag. Negatively stained images of representative particles from samples of P22- Δ MA-Gag assembled on templates with a) inward ssDNA strands and b) outward ssDNA strands. c) Box plots of the diameters measured for >50 particles in each set.

P22- Δ MA-Gag VLPs that upon Δ MA-Gag binding, ssDNA must collapse to a distribution located close to the P22 procapsid surface, without distortion of the relative arrangement of the principal domains of Gag. As suggested by chromatography, the inward DNA strand is closer to the final state of DNA in an assembled VLP, than the outward DNA strand. The latter will then require more compaction during the first steps of Δ MA-Gag binding. In other words, in the case of the outward DNA templates, additional work is required to bring the Δ MA-Gag molecules close to the procapsid surface, in comparison to the inward DNA templates. The additional work requirement is likely to lead to a less thermodynamically stable shell; hence, the presence of partial shells with defects.

Whatever the mechanism, a central role in this difference is played by the DNA and Δ MA-Gag binding event, which must trigger a conformational change to pull down Gag and generate VLPs of the final diameter.

Indeed, we find that when the nucleic acid link between the P22 procapsid and a complete Δ MA-Gag shell is removed through nuclease exposure, the VLP expands and obvious gaps in the Δ MA-Gag shell are introduced. In fact, occasionally, the gap is large enough to allow the P22 particle to completely leave the lumen of the Gag shell (Figure 7a,b). Interestingly, the empty Δ MA-Gag shell is metastable; we have observed well-formed shells stable *in vitro* for hours after the ssDNA was removed. This clearly shows that there are attractive forces acting at the Δ MA-Gag assembly interface, even in absence of DNA. This observation could be of significance for the non-diffusional phase transition model for maturation of HIV-1 recently proposed by Frank et al.^[53]

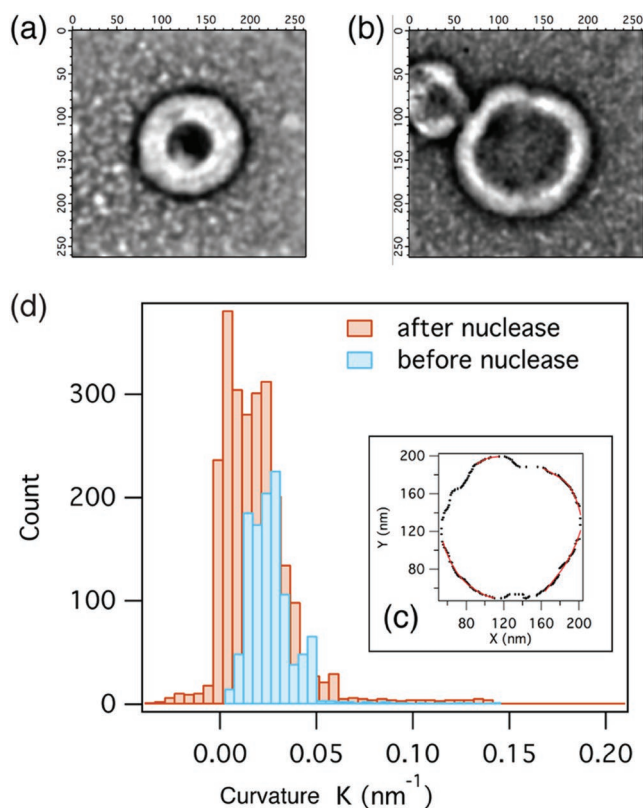


Figure 7. Nuclease-treatment of P22- Δ MA-Gag. Representative images of P22- Δ MA-Gag particles a) before and b) after digestion with nuclease. c) Dots: continuous arcs selected from the TEM image of digested P22- Δ MA-Gag (shown in panel (b)) fit using polynomial curves (red). Curvature was then calculated at each interpolation point based on polynomial fit coefficients. d) Histogram of radii of curvature (K) of arcs selected from particles before (blue) and after (orange) nuclease digestion.

We assessed the effect of nuclease digestion upon particle structure as follows: The DNA-free metastable shell was analyzed for local curvature by fitting a 5th order polynomial function to each continuous arc sector of the shell (Figure 7c). A histogram of local curvature was generated for each particle and histograms obtained from five particles were averaged together and compared with similar histograms obtained from VLPs prior to nuclease exposure. This analysis suggests that local curvature decreased significantly upon nuclease treatment (Figure 7d). After nuclease treatment the most frequent curvature was 0.004 nm^{-1} (corresponding to a radius of 250 nm) while before nuclease treatment, the most frequent curvature was 0.024 nm^{-1} (corresponding to a radius of 42 nm). Therefore, the nucleic acid plays an important role in governing the curvature of the Gag shell.^[46] Moreover, in the absence of DNA, Gag has an intrinsic curvature that is not only greater than the one imposed by the P22 template, but evidently greater than the mean curvature of most wt HIV particles. As a consequence, a Gag shell assembled around nucleic acid is most likely under bending strain regardless of the radius of the particle. This is important, because the magnitude of elastic strain relative to that of attractive interactions will dictate growth kinetics, and may play an important role in defining incompleteness in immature HIV-1.

3. Conclusion

Assembly of Gag molecules on a quasispherical template provided by P22 VLPs presents a novel approach to 2D spherical crystallography of proteins. We found that P22- Δ MA-Gag VLPs assembled in this way strongly resemble wt immature HIV-1 with respect to the radial and polar organization of Gag. However, an intriguing difference between P22- Δ MA-Gag VLPs and wt immature HIV-1 is that P22- Δ MA-Gag VLPs do not appear to include any large gaps. Further structural investigation of the global organization of Gag in P22- Δ MA-Gag will be of great interest since it will allow us to determine the nature of the defects that permit the hexameric lattice to close. The nature of the defects in turn should shed light on the local interactions between Gag subunits, which are difficult to analyze by other methods. The experiments with various ssDNA strands show that charge density is the primary determinant of Gag assembly. While the precise interactions required for stabilizing a Gag lattice remain to be identified, P22- Δ MA-Gag VLPs provide a starting point for a study, which will enable further investigations of the role of elastic strain in Gag assembly.

4. Experimental Section

Expression and Purification of P22 VLPs: The procapsid of bacteriophage P22 was genetically modified to incorporate surface cysteines by introducing a point mutation M338C in its coat protein. According to previous cryo-EM reconstructions of the P22 procapsid^[49] and more recent NMR domain structures,^[54] M338 is located in the surface-exposed I-domain of the coat protein (Supporting Information Figure S1). M338 was chosen since it was anticipated to be at the far C-terminus of the I-domain and not involved in intersubunit contacts predicted to occur through the I-domain.^[54] P22 procapsid VLPs were generated upon recombinant expression of the M338C coat protein and the wt scaffolding protein in BL21 *E. coli* as per O'Neil et al.^[55] Purified VLPs were stored at $4 \text{ }^\circ\text{C}$ in $50 \times 10^{-3} \text{ M}$ phosphate buffer at pH 7.

Functionalization of P22 VLPs with DNA: Surface lysines on the P22 procapsid VLPs were conjugated to a long-chain crosslinker, Sulfo-succinimidyl 6-(3'-(2-pyridyldithio)propionamido)hexanoate or Sulfo-LC-SPDP (Thermo Scientific), via an *N*-hydroxysuccinimide (NHS)-ester linkage to generate pyridyldithiol reactive groups. The disulfides in these pyridyldithiol groups were reduced using $50 \times 10^{-3} \text{ M}$ DTT (Sigma Aldrich) and thiols thus generated, as well as those from surface cysteines were used for functionalization of the procapsids with ssDNA.

ssDNA with 12 Nucleotides: 5'-ACACACACACAC-3' with an amine modification at the 5' end and 6-carboxyfluorescein at the 3' end was synthesized by Integrated DNA Technologies (IDT). Using an approach described by Williams and Chaput,^[56] ssDNA was chemically conjugated to surface thiols on procapsids via a crosslinker called Sulfo-succinimidyl 4-(*N*-maleimidomethyl)-cyclohexane-1-carboxylate or Sulfo-SMCC (Thermo Scientific). Conjugation reactions were conducted in $50 \times 10^{-3} \text{ M}$ phosphate buffer at pH 7 using 5 molar equivalents of ssDNA per coat protein. Functionalized procapsids were subsequently purified by size exclusion. The efficiency of ssDNA labeling of procapsids was calculated

using Equation (1), where (i) the concentration of ssDNA is calculated from the absorbance of the sample at 495 nm due to 6-carboxyfluorescein attached to each ssDNA (extinction coefficient = $75\,000\text{ M}^{-1}\text{ cm}^{-1}$), (ii) the concentration of coat proteins is calculated from the absorbance of the sample at 280 nm (extinction coefficient of P22 coat protein = $65\,700\text{ M}^{-1}\text{ cm}^{-1}$) after deducting contributions from the ssDNA, and (iii) the values are adjusted for the number of coat proteins per procapsid = 420

$$\text{Efficiency of procapsid labeling} = \frac{A_{495}/75000}{(A_{280} - 1.4 \times A_{495})/65700} \times 420 \quad (1)$$

To achieve the optimal nucleic acid concentration and charge density for Gag assembly, longer strands of ssDNA consisting of GT repeats (synthesized by IDT and listed in Supporting Information Table S1) were hybridized to the short AC strands on the procapsids via base pairing, upon incubation of the AC-labeled procapsids with equimolar amounts of GT-ssDNA at room temperature. Excess (unhybridized) ssDNA was removed using centrifugal filter units with a 100 kDa cutoff (Amicon). Of all the sequences of GT strands tested (Supporting Information Table S1), the optimal sequence for efficient assembly of Gag was found to be of 80 nucleotides: 5'-(GT)₁₀(GGTT)₁₅-3'.

Assembly of Δ MA-Gag on Templates of Functionalized P22 VLPs: Recombinant Δ MA-Gag^[57] was produced in BL21 *E. coli* and purified in high-salt buffer ($500 \times 10^{-3}\text{ M NaCl}$; $50 \times 10^{-3}\text{ M HEPES}$ at pH 7.5) conditions as per Datta and Rein.^[43] In vitro assembly reactions were initiated by diluting Δ MA-Gag to a final concentration of 1 mg mL^{-1} and adding functionalized P22 VLPs to a final ssDNA:Gag ratio of 3%–5% (w/w). Assembly was allowed to occur by lowering the salt concentration by dialysis of the mixture overnight at 4 °C against a low salt buffer ($75 \times 10^{-3}\text{ M NaCl}$; $25 \times 10^{-3}\text{ M Tris}$ at pH 7.5) using a cellulose membrane with an MW cutoff of 12–14 kDa (Spectrum Laboratories). The efficiency of assembly for each reaction was calculated from EM images using Equation (2)

$$\text{Efficiency of Assembly} = \frac{\text{Number of complete P22 } \Delta\text{MA Gag VLPs}}{\text{Total number of P22 particles}} \times 100\% \quad (2)$$

Transmission Electron Microscopy (TEM): For negative-stained EM, samples (typically 0.1 mg mL^{-1} protein in $50 \times 10^{-3}\text{ M}$ phosphate buffer pH 7) were adsorbed on carbon-coated copper grids (mesh size: 400; Electron Microscopy Sciences) by floating the grid on a droplet of sample for 10 min. The adsorbed sample was negatively stained by applying a 2% (w/v) uranyl acetate solution to the grid for 1 min. Excess sample and stain was removed using filter paper and the grids were air-dried before imaging. Images were acquired at an accelerating voltage of 80 kV on a JEOL 1010 transmission electron microscope equipped with a Gatan 4 k × 4 k CCD camera.

For cryo-EM, samples were applied to glow-discharged Quantifoil grids (R 1.2/1.3, mesh size: 300; Electron Microscopy Sciences) and plunge-frozen in liquid ethane using a Vitrobot Mark III (FEI). Cryo-images were collected using a JEOL JEM 3200FS electron microscope at an accelerating voltage of 300 kV and a magnification of $40\,000\times$ (corresponding to $2.9566\text{ \AA pixel}^{-1}$) using a Gatan UltraScan 4000 CCD camera. For cryo-reconstructions of functionalized P22, ≈ 90 images were collected manually. 1025 particles from these images were used for reconstruction utilizing the Auto3DEM software suite^[58] and PDB ID: 2XYX.^[49] Individual

particle visualization, averaging, and further manipulations were performed using EMAN1.^[59]

EM images were analyzed using ImageJ (NIH) for the measurement of particle diameters and Igor Pro (Wavemetrics) for the measurement of curvature, generation of line profiles, and Fourier transforms. Spider & Web software^[60] was used for conversion of images to polar coordinates.

Small Angle X-Ray Scattering (SAXS): The X-ray scattering data were collected at the P12 beamline of the European Molecular Biology Laboratory (EMBL)^[61] at the storage ring Petra III of the Deutsches Elektronen Synchrotron (DESY, Hamburg). Using a Pilatus2M detector, the scattering was recorded in the range of the momentum transfer $0.03\text{ nm}^{-1} < s < 4.5\text{ nm}^{-1}$, where $s = 4\pi \sin\theta/\lambda$, 2θ is the scattering angle, and $\lambda = 0.1\text{ nm}$ is the X-ray wavelength. The total exposure time per sample was set to 1 s (20 frames of 0.05 ms each) and the sample was loaded in a quartz capillary under vacuum to diminish parasitic scattering. After the subtraction of background scattering from the solvent, the SAXS curves were processed using PRIMUS.^[62] The distance distribution function $P(r)$ was calculated using indirect Fourier transform methods implemented by the program GNOM.^[63] The scattering from P22 was computed by CRY SOL^[64] and the modeling of polydispersity was conducted using MIXTURE.^[62]

The low-resolution shape of P22- Δ MA-Gag was reconstructed ab initio from the scattering patterns by MONSA.^[65] This program represents the object as an assembly of beads inside a spherical search volume. Starting from a random assembly, MONSA employed simulated annealing to build compact scattering equivalent models fitting the experimental data $I_{\text{exp}}(s)$ to minimize discrepancy

$$\Delta = \frac{1}{N-1} \sum_j \left[\frac{I_{\text{exp}}(s_j) - cI_{\text{calc}}(s_j)}{\sigma(s_j)} \right]^2 \quad (3)$$

where N is the number of experimental points, c is a scaling factor, and $I_{\text{calc}}(s_j)$ and $\sigma(s_j)$ are the calculated intensity from the model and the experimental error at the momentum transfer s_j , respectively. The program allows modeling of multiphase systems and simultaneous fitting of multiple curves.

The initialization of the search volume was done defining three phases (i.e., solvent, P22 VLPs, and P22- Δ MA-Gag VLPs) and dividing the search into three regions: (i) Inner core, phases allowed 0 and 1 (i.e., solvent or P22), radius 24 nm; (ii) inner shell, phases allowed 1 and 2 (i.e., P22 or P22- Δ MA-Gag), radius 30.5 nm; and (iii) outer shell, phases allowed 0 and 2 (i.e., solvent or P22- Δ MA-Gag), radius 52.5 nm. The two data sets collected for P22 and P22- Δ MA-Gag assembly were fitted simultaneously by a single multiphase ab initio model (chi-squared = 2.8).

Charge-Detection Mass Spectrometry (CDMS): Mass spectra were measured using a home-built single-molecule charge detection mass spectrometer that has been described previously.^[66] In short, electrospray ionization introduced ions into the gas phase. The gas phase ions entered the instrument through a heated metal capillary, which also aided in desolvation. Ions then passed through three differentially pumped regions where an RF ion funnel, an RF hexapole, and an RF quadrupole resided. After the quadrupole, ions were accelerated through a 100 V potential and focused into a kinetic energy analyzer. The kinetic energy analyzer separated ions based

on their energy per charge. Only ions within a narrow range of kinetic energies per charge were transmitted into the next region that contained a modified cone trap which housed a charge detection cylinder. A single ion was captured in the cone trap and oscillated for 95 ms. The image charge on the charge cylinder was amplified, digitized, and sent to a computer where the signal was analyzed using a fast Fourier transform (FFT). The fundamental frequency and first harmonic are used to derive the m/z of the ion while the magnitude of the FFT is used to obtain the ion charge (z). Masses are calculated by multiplying the m/z and z of each ion. The resulting masses are binned to obtain spectra. Further details about signal processing can be found elsewhere.^[67–69] Prior to CDMS, samples were buffer exchanged into 100×10^{-3} M ammonium acetate.

Gel Electrophoresis: Templates were routinely characterized by electrophoresis on 0.7% (w/v) agarose gels in $1 \times$ TAE buffer (pH = 8.3). Typically, ≈ 10 μ g VLP sample was mixed with $2 \times$ gel loading buffer and electrophoresed at 60 V for 2 h. To visualize VLPs, the samples were fixed by incubating the gel in Coomassie Brilliant Blue solution (BioRad) for 20 min, followed by destaining overnight and imaging in white light. To check for the presence of DNA in the sample, the gel was placed in 0.5 μ g mL⁻¹ ethidium bromide for 10 min and imaged under UV light.

Nuclease Digestion of VLPs: For digestion of DNA attached to template cores of VLPs, assembled VLPs were digested with Deoxyribonuclease (DNase) I (New England Biolabs) in a Tris-buffer at pH = 7.5 containing 2.5×10^{-3} M MgCl₂ and 0.5×10^{-3} M CaCl₂, as per the manufacturer's recommendations. The digestion was allowed to continue at room temperature for up to 48 h. Samples were collected at six-hourly time points and dried on grids for visualization by TEM. DNase I was inactivated by a change in pH upon addition of the staining solution to grids prior to TEM.

Supporting Information

Supporting Information is available from the Wiley Online Library or from the author.

Acknowledgements

P.S. and L.H. contributed equally to this work. The authors gratefully acknowledge Dr. John A. G. Briggs (European Molecular Biology Laboratory, Heidelberg, Germany) and Dr. Peter E. Prevelige Jr. (Department of Microbiology, University of Alabama, Birmingham, USA) for insightful discussions on this project. The IU Nanoscale Characterization Facility is thanked for access to instrumentation. This work was supported by the Human Frontier Science Program research grant RGP0017/2012 (to B.D., A.R., D.S., and Dr. Paul van der Schoot, Technische Universiteit Eindhoven, The Netherlands) for work on cryo-EM, SAXS, molecular biology and numerical simulations; by the Intramural Research Program of the NIH, National Cancer Institute, Center for Cancer Research (to A.R.); and by the U.S. Department of Energy, Office of Science, Basic Energy Sciences, under award DE-SC0010507 (to B.D.) for work on data processing algorithms.

- [1] R. F. Bruinsma, W. M. Gelbart, D. Reguera, J. Rudnick, R. Zandi, *Phys. Rev. Lett.* **2003**, *90*, 248101.
- [2] A. Zlotnick, *J. Mol. Recognit.* **2005**, *18*, 479.
- [3] W. H. Roos, R. Bruinsma, G. J. L. Wuite, *Nat. Phys.* **2010**, *6*, 733.
- [4] A. M. Wen, P. H. Rambhia, R. H. French, N. F. Steinmetz, *J. Biol. Phys.* **2013**, *39*, 301.
- [5] M. G. Mateu, *Arch. Biochem. Biophys.* **2013**, *531*, 65.
- [6] L. He, Y. Liu, J. Liu, Y. Xiong, J. Zheng, Y. Liu, Z. Tang, *Angew. Chem., Int. Ed. Engl.* **2013**, *52*, 3741.
- [7] Z. Li, Z. Zhu, W. Liu, Y. Zhou, B. Han, Y. Gao, Z. Tang, *J. Am. Chem. Soc.* **2012**, *134*, 3322.
- [8] Y. Xia, T. D. Nguyen, M. Yang, B. Lee, A. Santos, P. Podsiadlo, Z. Tang, S. C. Glotzer, N. A. Kotov, *Nat. Nanotechnol.* **2011**, *6*, 580.
- [9] Z. Zhu, H. Meng, W. Liu, X. Liu, J. Gong, X. Qiu, L. Jiang, D. Wang, Z. Tang, *Angew. Chem., Int. Ed. Engl.* **2011**, *50*, 1593.
- [10] R. Zandi, D. Reguera, R. F. Bruinsma, W. M. Gelbart, J. Rudnick, *Proc. Natl. Acad. Sci. USA* **2004**, *101*, 15556.
- [11] D. L. Caspar, A. Klug, *Cold Spring Harbor Symp. Quant. Biol.* **1962**, *27*, 1.
- [12] A. Zlotnick, S. J. Stray, *Trends Biotechnol.* **2003**, *21*, 536.
- [13] D. Endres, A. Zlotnick, *Biophys. J.* **2002**, *83*, 1217.
- [14] J. Lidmar, L. Mirny, D. R. Nelson, *Phys. Rev. E: Stat., Nonlinear, Soft Matter Phys.* **2003**, *68*, 051910.
- [15] R. Schwartz, P. W. Shor, P. E. Prevelige Jr., B. Berger, *Biophys. J.* **1998**, *75*, 2626.
- [16] W. I. Sundquist, H. G. Krausslich, *Cold Spring Harbor Perspect. Med.* **2012**, *2*, a006924.
- [17] P. E. Prevelige, *J. Mol. Biol.* **2011**, *410*, 634.
- [18] T. Wilk, I. Gross, B. E. Gowen, T. Rutten, F. de Haas, R. Welker, H. G. Krausslich, P. Boulanger, S. D. Fuller, *J. Virol.* **2001**, *75*, 759.
- [19] S. D. Fuller, T. Wilk, B. E. Gowen, H. G. Krausslich, V. M. Vogt, *Curr. Biol.* **1997**, *7*, 729.
- [20] J. Wagner, G. Erdemci-Tandogan, R. Zandi, *J. Phys.: Condens. Matter* **2015**, *27*, 495101.
- [21] G. Meng, J. Paulose, D. R. Nelson, V. N. Manoharan, *Science* **2014**, *343*, 634.
- [22] M. J. Bowick, D. R. Nelson, H. Shin, *Phys. Chem. Chem. Phys.* **2007**, *9*, 6304.
- [23] J. A. Briggs, J. D. Riches, B. Glass, V. Bartonova, G. Zanetti, H. G. Krausslich, *Proc. Natl. Acad. Sci. USA* **2009**, *106*, 11090.
- [24] B. K. Ganser-Pornillos, M. Yeager, O. Pornillos, *Adv. Exp. Med. Biol.* **2012**, *726*, 441.
- [25] B. K. Ganser-Pornillos, M. Yeager, W. I. Sundquist, *Curr. Opin. Struct. Biol.* **2008**, *18*, 203.
- [26] J. A. Briggs, H. G. Krausslich, *J. Mol. Biol.* **2011**, *410*, 491.
- [27] S. A. Datta, Z. Zhao, P. K. Clark, S. Tarasov, J. N. Alexandratos, S. J. Campbell, M. Kvaratskhelia, J. Lebowitz, A. Rein, *J. Mol. Biol.* **2007**, *365*, 799.
- [28] N. Yu, M. F. Hagan, *Soft Condens. Matter* **2015**, arXiv:1506.08747v2.
- [29] A. de Marco, N. E. Davey, P. Ulbrich, J. M. Phillips, V. Lux, J. D. Riches, T. Fuzik, T. Ruml, H. G. Krausslich, V. M. Vogt, J. A. Briggs, *J. Virol.* **2010**, *84*, 11729.
- [30] L. A. Carlson, J. A. Briggs, B. Glass, J. D. Riches, M. N. Simon, M. C. Johnson, B. Muller, K. Grunewald, H. G. Krausslich, *Cell Host Microbe* **2008**, *4*, 592.
- [31] A. R. Bausch, M. J. Bowick, A. Cacciuto, A. D. Dinsmore, M. F. Hsu, D. R. Nelson, M. G. Nikolaidis, A. Travesset, D. A. Weitz, *Science* **2003**, *299*, 1716.
- [32] F. K. Schur, W. J. Hagen, M. Rumlova, T. Ruml, B. Muller, H. G. Krausslich, J. A. Briggs, *Nature* **2014**, *517*, 505.
- [33] R. Zandi, P. van der Schoot, *Biophys. J.* **2009**, *96*, 9.
- [34] T. A. Bharat, L. R. Castillo Menendez, W. J. Hagen, V. Lux, S. Igonet, M. Schorb, F. K. Schur, H. G. Krausslich, J. A. Briggs, *Proc. Natl. Acad. Sci. USA* **2014**, *111*, 8233.
- [35] T. A. Bharat, N. E. Davey, P. Ulbrich, J. D. Riches, A. de Marco, M. Rumlova, C. Sachse, T. Ruml, J. A. Briggs, *Nature* **2012**, *487*, 385.

- [36] N. L. Goicochea, S. A. Datta, M. Ayaluru, C. Kao, A. Rein, B. Dragnea, *J. Mol. Biol.* **2011**, *410*, 667.
- [37] G. Yu, R. Yan, C. Zhang, C. Mao, W. Jiang, *Small* **2015**, *11*, 5157.
- [38] S. Kang, M. Uchida, A. O'Neil, R. Li, P. E. Prevelige, T. Douglas, *Biomacromolecules* **2010**, *11*, 2804.
- [39] P. E. Prevelige Jr., D. Thomas, J. King, *J. Mol. Biol.* **1988**, *202*, 743.
- [40] E. R. Wright, J. B. Schooler, H. J. Ding, C. Kieffer, C. Fillmore, W. I. Sundquist, G. J. Jensen, *EMBO J.* **2007**, *26*, 2218.
- [41] S. Campbell, R. J. Fisher, E. M. Towler, S. Fox, H. J. Issaq, T. Wolfe, L. R. Phillips, A. Rein, *Proc. Natl. Acad. Sci. USA* **2001**, *98*, 10875.
- [42] I. Gross, H. Hohenberg, T. Wilk, K. Wieggers, M. Grattinger, B. Muller, S. Fuller, H. G. Krausslich, *EMBO J.* **2000**, *19*, 103.
- [43] S. A. Datta, A. Rein, *Methods Mol. Biol.* **2009**, *485*, 197.
- [44] S. Campbell, A. Rein, *J. Virol.* **1999**, *73*, 2270.
- [45] D. Muriaux, J. Mirro, D. Harvin, A. Rein, *Proc. Natl. Acad. Sci. USA* **2001**, *98*, 5246.
- [46] C. Faivre-Moskalenko, J. Bernaud, A. Thomas, K. Tartour, Y. Beck, M. Iazykov, J. Danial, M. Lourdin, D. Muriaux, M. Castelnovo, *PLoS One* **2014**, *9*, e83874.
- [47] F. Sausset, G. Tarjus, D. R. Nelson, *Phys. Rev. E: Stat., Nonlinear, Soft Matter Phys.* **2010**, *81*, 031504.
- [48] W. D. Luedtke, U. Landman, *J. Phys. Chem. B* **1998**, *102*, 6566.
- [49] D. H. Chen, M. L. Baker, C. F. Hryc, F. DiMaio, J. Jakana, W. Wu, M. Dougherty, C. Haase-Pettingell, M. F. Schmid, W. Jiang, D. Baker, J. A. King, W. Chiu, *Proc. Natl. Acad. Sci. USA* **2011**, *108*, 1355.
- [50] J. A. Briggs, M. N. Simon, I. Gross, H. G. Krausslich, S. D. Fuller, V. M. Vogt, M. C. Johnson, *Nat. Struct. Mol. Biol.* **2004**, *11*, 672.
- [51] A. G. Stephen, S. A. Datta, K. M. Worthy, L. Bindu, M. J. Fivash, K. B. Turner, D. Fabris, A. Rein, R. J. Fisher, *J. Biomol. Tech.* **2007**, *18*, 259.
- [52] H. Wu, I. Rouzina, M. C. Williams, *RNA Biol.* **2010**, *7*, 712.
- [53] G. A. Frank, K. Narayan, J. W. Bess Jr., G. Q. Del Prete, X. Wu, A. Moran, L. M. Hartnell, L. A. Earl, J. D. Lifson, S. Subramaniam, *Nat. Commun.* **2015**, *6*, 5854.
- [54] A. A. Rizzo, M. M. Suhanovsky, M. L. Baker, L. C. Fraser, L. M. Jones, D. L. Rempel, M. L. Gross, W. Chiu, A. T. Alexandrescu, C. M. Teschke, *Structure* **2014**, *22*, 830.
- [55] A. O'Neil, C. Reichhardt, B. Johnson, P. E. Prevelige, T. Douglas, *Angew. Chem., Int. Ed. Engl.* **2011**, *50*, 7425.
- [56] B. A. Williams, J. C. Chaput, in *Current Protocols in Nucleic Acid Chemistry*, John Wiley and Sons Inc, USA **2010**, DOI: 10.1002/0471142700.nc0441s42.
- [57] I. Gross, H. Hohenberg, H. G. Krausslich, *Eur. J. Biochem.* **1997**, *249*, 592.
- [58] X. Yan, R. S. Sinkovits, T. S. Baker, *J. Struct. Biol.* **2007**, *157*, 73.
- [59] S. J. Ludtke, P. R. Baldwin, W. Chiu, *J. Struct. Biol.* **1999**, *128*, 82.
- [60] J. Frank, M. Radermacher, P. Penczek, J. Zhu, Y. Li, M. Ladjaj, A. Leith, *J. Struct. Biol.* **1996**, *116*, 190.
- [61] C. E. Blanchet, A. Spilotros, F. Schwemmer, M. A. Graewert, A. Kikhney, C. M. Jeffries, D. Franke, D. Mark, R. Zengerle, F. Cipriani, S. Fiedler, M. Roessle, D. I. Svergun, *J. Appl. Crystallogr.* **2015**, *48*, 431.
- [62] P. V. Konarev, V. V. Volkov, A. V. Sokolova, M. H. J. Koch, D. I. Svergun, *J. Appl. Crystallogr.* **2003**, *36*, 1277.
- [63] D. I. Svergun, *J. Appl. Crystallogr.* **1992**, *25*, 495.
- [64] D. Svergun, C. Barberato, M. H. J. Koch, *J. Appl. Crystallogr.* **1995**, *28*, 768.
- [65] D. I. Svergun, *Biophys. J.* **1999**, *76*, 2879.
- [66] N. C. Contino, E. E. Pierson, D. Z. Keifer, M. F. Jarrold, *J. Am. Soc. Mass Spectrom.* **2013**, *24*, 101.
- [67] E. E. Pierson, D. Z. Keifer, L. Selzer, L. S. Lee, N. C. Contino, J. C. Wang, A. Zlotnick, M. F. Jarrold, *J. Am. Chem. Soc.* **2014**, *136*, 3536.
- [68] E. E. Pierson, N. C. Contino, D. Z. Keifer, M. F. Jarrold, *J. Am. Soc. Mass Spectrom.* **2015**, *26*, 1213.
- [69] D. Z. Keifer, E. E. Pierson, J. A. Hogan, G. J. Bedwell, P. E. Prevelige, M. F. Jarrold, *Rapid Commun. Mass Spectrom.* **2014**, *28*, 483.

Received: May 20, 2016
Revised: August 5, 2016
Published online: September 16, 2016